Atom-resolved noncontact atomic force microscopic and scanning tunneling microscopic observations of the structure and dynamic behavior of CeO$_2$(1 1 1) surfaces

Yoshimichi Namai, Ken-Ichi Fukui[1], Yasuhiro Iwasawa[*]

Department of Chemistry, Graduate School of Science, The University of Tokyo, 7-3-1 Hongo, Bunkyo-ku, Tokyo 113-0033, Japan

Abstract

Atomic-scale structures and dynamic behaviors of CeO$_2$(1 1 1) surfaces were imaged by noncontact atomic force microscopy (NC-AFM) and scanning tunneling microscopy (STM). Hexagonally arranged oxygen atoms, oxygen point vacancies, multiple oxygen vacancies, and hydrogen adatoms at the surfaces were visualized by atom-resolved NC-AFM observations. Multiple defects were stabilized by displacement of the surrounding oxygen atoms around the multiple defects, which gave enhanced brightness in the NC-AFM image due to a geometric reason. Multiple defects without reconstruction of the surrounding oxygen atoms were reactive and were healed by exposure to O$_2$ gas and methanol at RT. Successive NC-AFM and STM measurements of slightly reduced CeO$_2$(1 1 1) surfaces revealed that hopping of surface oxygen atoms faced to the metastable multiple defects was thermally activated even at room temperature (RT) and more promoted at higher temperatures. Heterogeneous feature of the reactivity of surface oxygen atoms with methanol was imaged by successive NC-AFM observations. These observations gave a new insight for understanding the surface structures and behavior of CeO$_{2-x}$ with the facile oxygen reservoir and oxidation–reduction properties related to the unique catalysis.
© 2003 Elsevier B.V. All rights reserved.

1. Introduction

Cerium oxide (CeO$_2$) have been known to have high oxygen transport and storage capacities, and used in industrial applications to catalysts, fuel cells, and oxygen sensors [1–3]. Cerium oxides (CeO$_{2-x}$, $0 \leq x \leq 0.5$) have been most widely used as an active component in three-way catalysts for automobile exhaust gas treatments, where they play a crucial role as an 'oxygen storage' component to control the oxygen concentration at catalyst surfaces [3]. Cerium oxides also show unique activities for various catalytic reactions such as CO oxidation, selective oxidation of hydrocarbons, oxidative coupling of methane, water gas shift reaction, and removal of SO$_x$ from fluid catalytic cracking (FCC) flue gases [2,4–6].

CeO$_2$ has a cubic fluorite (CaF$_2$) structure with a lattice constant of 0.541 nm. CeO$_2$ at its stoichiometric composition is an electrically insulating

* Corresponding author. Tel.: +81-3-5841-4363;
fax: +81-3-5800-6892.
E-mail address: iwasawa@chem.s.u-tokyo.ac.jp (Y. Iwasawa).
[1] Present address: Department of Chemistry, Graduate School of Science and Engineering, Tokyo Institute of Technology, Okayama, Meguro-ku, Tokyo 152-8550, Japan.

f-transition metal oxide with a wide band gap of ca. 6 eV [7]. Since the lattice constant of CeO_2 is almost the same as that of Si (0.543 nm), the application of CeO_2 as an insulating buffer layer between Si surface and high-temperature super conducting oxide thin films has also attracted attention [8].

Despite the importance of these technological applications, few studies on cerium oxide single crystal surfaces have been reported as yet. Theoretical energy calculations of a CeO_2 surface indicated that a (1 1 1) surface is the most stable surface among the low index planes [9,10]. Cerium oxide surfaces have been studied by X-ray photoelectron spectroscopy (XPS), ultraviolet photoelectron spectroscopy (UPS), and high-resolution electron energy loss spectroscopy (HREELS) [7]. However, direct observations of atomic-scale surface structures and dynamic behaviors of surface oxygen atoms of CeO_{2-x} are inevitable to understand the key property of cerium oxides in the various applications.

Oxygen deficiencies lead to the reduction of Ce^{4+} to Ce^{3+} and to occupation of the empty states left in the band gap [7]. Thus, CeO_{2-x} becomes conductive to some extent by creating oxygen vacancies in the bulk. Actually, surface structures of a reduced nonstoichiometric $CeO_{2-x}(1 1 1)$ were investigated by scanning tunneling microscopy (STM) at room temperature (RT) with tunneling current as low as 10 pA or at elevated temperatures of 573–773 K to increase the electronic conductivity of the substrate [11,12]. Surface reconstructions on $CeO_2(0 0 1)$ and $CeO_2(1 1 0)$ were also observed by STM [13,14]. However, it is very difficult to observe a nearly stoichiometric CeO_2 surface by STM. Noncontact atomic force microscopy (NC-AFM) is more favorable to image atomically cerium oxide surfaces independent of the oxidation states. Since the first report of atom-resolved NC-AFM images of $TiO_2(1 1 0)$-(1×1) with oxygen point defects [15], several atom-resolved images of oxide surfaces have been reported on $TiO_2(1 0 0)$ [16], $SnO_2(1 1 0)$ [17], and $NiO(1 0 0)$ [18]. NC-AFM observations of the atomic structure on α-$Al_2O_3(0 0 0 1)$ surface were also reported [19]. Besides, it has been shown that NC-AFM can be applied to monitor dynamic processes of atoms [20] and molecules [21] on surfaces.

We have studied atomic-level structures and behavior of oxygen atoms of $CeO_2(1 1 1)$ surfaces depending on the oxidation states by NC-AFM [22,23]. Hexagonally arranged oxygen atoms, oxygen point vacancies, and multiple oxygen vacancies such as triangular defects and line defects on the surfaces were visualized by NC-AFM in atomic scale. We concluded that the $CeO_2(1 1 1)$ surface is oxygen-terminated. Successive NC-AFM measurements of the same area of a slightly reduced $CeO_2(1 1 1)$ surface revealed that hopping of surface oxygen atoms faced to metastable multiple defects was thermally activated even at RT.

In the present paper, we report the atom-resolved NC-AFM images of a nearly stoichiometric CeO_2 (1 1 1) surface, and oxygen defects and hydrogen adatoms at $CeO_{2-x}(1 1 1)$ surfaces. Dynamic processes of oxygen atoms on $CeO_{2-x}(1 1 1)$ surfaces under vacuum, oxygen, and methanol were also visualized by in situ NC-AFM and STM observations.

2. Experimental

The NC-AFM and STM experiments were performed in an ultrahigh vacuum (UHV) AFM/STM (JEOL JAFM4500XT) equipped with an ion gun, a low energy electron diffraction (LEED) optics, and an XPS electron energy analyzer (VG Scientific CLAM2) with an Mg Kα X-ray source. The base pressure in the measurement system was 1.0×10^{-8} Pa. A polished $CeO_2(1 1 1)$ sample of 5.5 mm $\times$ 1.2 mm $\times$ 0.95 mm (Commercial Crystal Laboratories) was cleaned by several cycles of Ar^+ ion sputtering (3 keV for 3 min) and UHV annealing at 1173 K for 60 s. After the cleaning procedure, the surface exhibited a (1×1) LEED pattern, and XPS measurements did not detect any trace of impurities such as calcium, which is a possible contaminant in bulk CeO_2. For NC-AFM measurements, stiff and conductive silicon cantilevers with f_0 = 250–350 kHz and k = 20–30 N m^{-1} (NT-MDT) were used as force sensors. Resonant frequency shift of the cantilever was detected by FM method [24]. Since the cantilevers were used without Ar^+ ion sputtering, we assumed that most of the surfaces of the Si tip were initially covered with a native oxide layer. The cantilevers after Ar^+ ion sputtering also indicated similar contrasts to those obtained by the cantilevers without Ar^+ ion sputtering. Topographic images were obtained by applying a voltage to the Z piezo to keep the negative frequency shift

constant during scanning the surfaces. Bias voltage (V_s) was applied to the sample between -0.17 and -0.93 V to compensate the average contact potential between the tip and the sample during imaging the surface by NC-AFM [25]. The amplitude of vibration of the cantilever was approximately 6 nm. STM measurements were performed by using an electrochemically etched W tip. Electrochemical preparation of W tip was performed with 2 N NaOH solution, which is most often used as an etching electrolyte. Bias voltage was applied in the range of -1.0 to -3.0 V. Topographic images were obtained by applying a voltage to the Z piezo to keep a constant of tunneling current during scanning the surfaces. Methanol (Wako Pure Chemicals, research grade) was purified by repeated freeze–pump–thaw cycles and introduced into the NC-AFM and STM chamber through a gas doser. All NC-AFM measurements were performed at RT. While STM measurements were performed in the temperature range from RT to 400 K.

3. Results and discussion

3.1. Oxygen-terminated CeO₂(1 1 1) surface

By annealing an Ar$^+$ ion-sputtered CeO$_2$(1 1 1) surface at 1173 K under UHV for 60 s, terraces developed as stacks of disks whose diameter ranged 10–100 nm [22]. Each terrace was separated by steps of multiples of 0.3 nm high, which corresponds to a separation at O–Ce–O layer components in bulk CeO$_2$ (0.313 nm). Surface energy calculations for CeO$_2$(1 1 1) showed that an oxygen termination at the top of the O–Ce–O layer is more stable than a Ce-layer termination [9,10]. It is partly because the oxygen termination at the top of the neutral O–Ce–O layer forms no dipole moment perpendicular to the surface. Fig. 1 shows typical atom-resolved NC-AFM image of a nearly stoichiometric CeO$_2$(1 1 1) surface. Hexagonally arranged bright spots with a constant separation of 0.38 ± 0.02 nm were atomically resolved. These are consistent with the (1×1) unit cell of the bulk-terminated CeO$_2$(1 1 1) structure [22,23]. From the energy calculation and the coordination number of exposed Ce^{4+} to O^{2-} on CeO$_2$(1 1 1) surface, CeO$_2$(1 1 1) surface is predicted to be oxygen-terminated. The previous STM studies
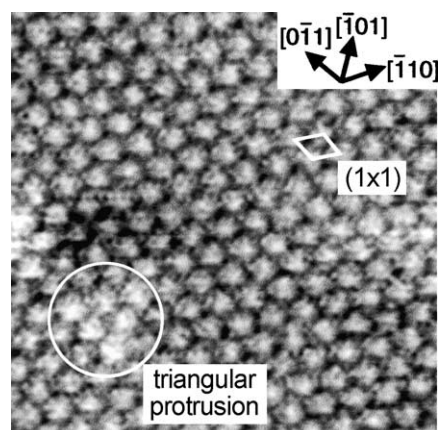

Fig. 1. Atom-resolved NC-AFM image of a nearly stoichiometric CeO$_2$(1 1 1) surface. 5.3 nm $\times$ 5.3 nm, $\Delta f \sim 112$ Hz. Hexagonally arranged bright contrasts and a triangular protrusion as brighter contrast are observed.

indicate that electrons are tunneling from occupied electronic states of CeO$_2$ which are derived mainly from O 2p orbital and hence that the filled-state images represent oxygen ions which form the topmost surface layer [11,26]. However, this was concluded from a premise that the topmost layer of (1 1 1) plane of fluorite-like oxides consists of oxygen to avoid a polar surface [11]. We have determined the topmost layer of the CeO$_2$(1 1 1) surface on the basis of the atom-resolved NC-AFM images of clean, oxygen-readsorbed, and methanol-adsorbed surfaces and an anisotropic orientation of triangular multiple defects [23]. Direct observation of an adsorption site of molecules by STM and NC-AFM has been used as a convincing method to determine the nature of bright contrasts and hence the surface structure of metal oxides. For example, imaging of individual adsorbed formate ions was used to probe surface Ti ions [27–29]. Recently, at a TiO$_2$(0 0 1) surface with fourfold coordinated and fivefold coordinated Ti atoms, methanol was used to identify the fourfold coordinated Ti atoms on the TiO$_2$(0 0 1) surface [30].

As shown in Fig. 1, triangular protrusions were also observed as brighter contrasts than other oxygen atoms on the nearly stoichiometric surface. The triangular protrusion enclosed by a circle was resolved into six bright spots whose apparent topographies were higher than other surface oxygen atoms by 0.03–0.05 nm, but the in-plane positions were almost identical to those

expected from the bulk-terminated structure. It is to be noted that they always pointed the same directions. Such triangular protrusions can be observed on the nearly stoichiometric $CeO_2(1\,1\,1)$ surface, while they were seldom observed on $CeO_2(1\,1\,1)$ surfaces with the density of oxygen vacancies above $5.0 \times 10^{12}\,cm^{-2}$. Thus the protruded structure may reflect local stress due to Coulombic repulsion between negatively charged oxygen anions. The local stress may be a key issue to form oxygen vacancies on the surface.

NC-AFM and STM measurements of cleaned $CeO_2(1\,1\,1)$ surfaces also revealed a protrusion as a brighter contrast. Fig. 2 shows an atom-resolved NC-AFM image of the protrusions. The height of the protrusions was 0.03–0.05 nm. The height was consistent with the height obtained by NC-AFM image for hydrogen adatoms on $TiO_2(1\,1\,0)$ surface, which were the same species as those reported by STM [31,32]. Thus the protrusion may be considered as hydrogen adatoms, adsorbed on top of the oxygen atom sites as evidenced in Fig. 2, where two of the protrusions are shown with mesh lines. The density of hydrogen adatoms on the $CeO_2(1\,1\,1)$ surface ranged from 0.01 to 0.03 ML ($1\,ML = 7.9 \times 10^{14}\,cm^{-2}$).

3.2. Surface defect structures

Oxygen point vacancies and multiple oxygen vacancies were observed as dark depressions in Figs. 2 and 3. When oxide surfaces are heated at elevated temperatures or exposed to ion beam under UHV, oxygen vacancies are formed as indicated from measurements of the electronic structure [33]. For a $CeO_2(1\,1\,1)$ surface annealed at 1173 K for 60 s, the density of the oxygen point defects was calculated to be $(0.8–1.7) \times 10^{12}\,cm^{-2}$ (0.1–0.2% of top layer O^{2-}). The density of surface oxygen vacancies increased with increasing annealing time at 1173 K. After annealing the surface at 1173 K for 120 s totally, the density of surface oxygen vacancies increased to $(5.3–7.9) \times 10^{12}\,cm^{-2}$ (0.6–1.0% of top layer O^{2-}) [22,23]. By further increasing the oxygen defect density to $(1.7–3.6) \times 10^{13}\,cm^{-2}$ (2.1–4.6% of top layer O^{2-}) by annealing at 1173 K for 240 s, multiple defects such as line defects and triangular defects appeared as shown in Fig. 3. Fig. 3(a) and (b) show point defect, line defect, and triangular defect imaged by NC-AFM. Oxygen point vacancies, which were exclusively observed
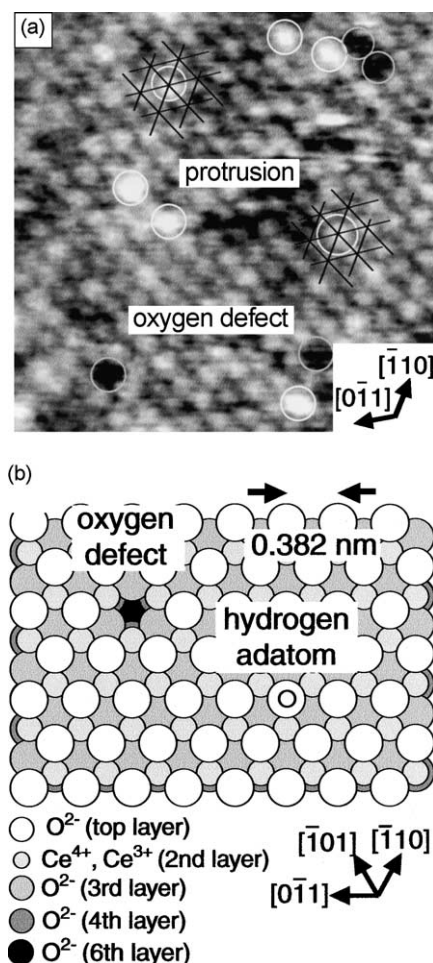

Fig. 2. (a) Atom-resolved NC-AFM image (5.8 nm × 5.8 nm) of a $CeO_2(1\,1\,1)$ surface with hydrogen adatoms ($\Delta f \sim 163\,Hz$). Hydrogen adatoms are observed at on-top sites of surface oxygen atoms. (b) A structural model of adsorption sites of the hydrogen adatom and point defect observed in (a).

by NC-AFM on the surfaces with an oxygen vacancy density below $1 \times 10^{13}\,cm^{-2}$, became minor ones. The multiple defects observed in Fig. 3(a) qualitatively reproduced previous STM observations on nonstoichiometric $CeO_{2-x}(1\,1\,1)$ [11,12]. The triangular defect consisted of three neighboring oxygen vacancies with a third layer oxygen atom at its centroid, while the line defects consisted of removal of oxygen atoms along the $[\bar{1}\,1\,0]$, $[\bar{1}\,0\,1]$, and $[0\,\bar{1}\,1]$ directions (Fig. 3(c)).

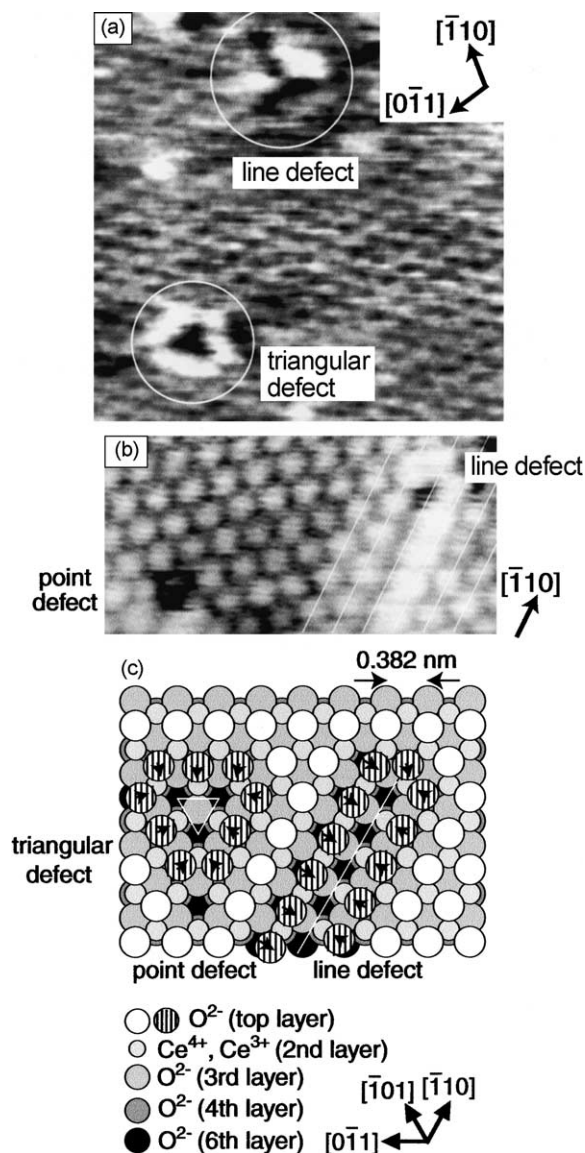Energy calculations of an oxygen point vacancy and two accompanying Ce^{3+} at different positions in the

Fig. 3. (a) NC-AFM image (5.7 nm × 5.7 nm) of a slightly reduced CeO$_2$(1 1 1) surface with multiple defects such as line defect and triangular defect ($\Delta f \sim 258$ Hz). (b) High resolution NC-AFM image (4.5 nm × 2.0 nm) including a point defect and a line defect observed on the same surface as (a) ($\Delta f \sim 171$ Hz). (c) A structural model of the displacement of oxygen atoms surrounding the line defect and triangular defects observed in (a).

bulk and at low index planes of CeO$_2$ indicated that the oxygen vacancy preferred the surface to the bulk and two Ce^{3+} occupied exposed surface sites associated with the oxygen vacancy [9,10]. Besides, associ-

ation of two surface oxygen vacancies side by side on CeO$_2$(1 1 1) was calculated to be energetically favored against two isolated point vacancies on the surface [10]. However, multiple defects were not observed on CeO$_2$(1 1 1) until the density of oxygen vacancies increased up to 1×10^{13} cm^{-2}. Formation of Ce^{3+} by reduction leads to occupation of vacant 4f states within the band gap for stoichiometric CeO$_2$ as is evident from spectroscopy such as XPS [7,34] and EELS [7].

Enhanced brightness at the edge oxygen atoms of triangular defects and line defects observed in the previous STM studies on CeO$_2$(1 1 1) was also observed by NC-AFM (Fig. 3(a)). The brighter contrasts were higher in topography than oxygen atoms far from the line defect by 0.05–0.08 nm, which was larger than the height difference of 0.03 nm reported by STM [11]. Based on the conventional view of reduction of two Ce^{4+} to two Ce^{3+} accompanied by an oxygen vacancy formation, six exposed Ce cations at the triangular defect and most of Ce cations exposed at the line defect ($2n$ of $(2n + 1)$ Ce cations for n-atom oxygen vacancies) are expected to be Ce^{3+}. Nörenberg and Briggs [11] attributed the enhanced brightness at the edge oxygen in the STM image to delocalization of electrons, which are otherwise supposed to be localized at Ce cations, to the surrounding oxygen anions.

By measurements of the multiple defects on CeO$_2$(1 1 1) with atomic-scale resolution by NC-AFM, we found that the multiple defects were accompanied by local reconstructed [22,23]. Atom-resolved NC-AFM images elucidated that the oxygen atoms surrounding the multiple defects were displaced toward the multiple defect sites as indicated by the arrows in Fig. 3(c). Fig. 3(b) shows a local reconstructed structure of the line defect. In this case, oxygen atoms only at the right-hand side of the line defect were observed with brighter contrast and displaced toward the defect by 0.05 nm. Note that it is not an artifact, for example, by delayed feedback during the measurements, because a point oxygen vacancy was observed without enhanced contrast around it at the bottom left in Fig. 3(b). As another type, oxygen atoms on both sides surrounding the line defect were observed with brighter contrast, where they were displaced toward the defect (Fig. 3(c)). Our STM measurements of multiple defects on nonstoichiometric CeO$_{2-x}$(1 1 1) also indicated that the enhanced brightness around the multiple defects was

always accompanied by in-plane displacement of the edge oxygen atoms. At the triangular defect, which was a minor multiple defect in our observations on slightly reduced $CeO_2(1\,1\,1)$ surfaces, oxygen atoms surrounding the defect showed an enhanced contrast as clearly shown in Fig. 3(a) and distorted towards the defect by 0.03–0.05 nm. It is to be noted that the direction of the triangular defect was always rotated by $60°$ from the triangular protrusion imaged in Fig. 1. Their in-plane positions are schematically shown in a model of Fig. 3(c), where only the first layer oxygen anions are displaced. These results are contradictory to the previous view that redistribution of electrons around the multiple defects is the reason for the brighter contrast around the multiple defects [11]. We consider that the displacement of oxygen atoms on the $(1\,1\,1)$ plane is the major reason for the brighter contrast. If redistribution of electrons to the oxygen atoms faced to the multiple defects occurs, different charge density on the oxygen anions should affect the interaction between the tip and the sample, which would lead to a different contrast on the NC-AFM image as shown by recent NC-AFM experiments and theoretical calculations [35]. If the amount of electrons redistributed to each edge oxygen atom surrounding the multiple defects depends on the number of the oxygen atoms per an oxygen vacancy, these should be reflected to the image contrast observed by STM or NC-AFM. However, such a tendency was not observed in our NC-AFM and STM measurements on oxygen defects on $CeO_2(1\,1\,1)$. If we simply postulate that only the first layer oxygen atoms with brighter contrast are displaced from the bulk-terminated positions, while fixing the distance to exposed Ce cations to 0.234 nm, which is the distance between the O atom and the Ce atom in the bulk oxygen atoms on the left-hand side and the right-hand side of the line defect in Fig. 3(c) will be lifted up by 0.06 and 0.08 nm, respectively. These values are nearly consistent with those observed by the present NC-AFM measurements. However, if the displacement is caused by a relaxation of the first layer oxygen to compensate the repulsion between oxygen anions at the first layer, a question remains why the second-nearest oxygen atoms from the line defects were not distorted. In considering the displacement structures, bulk Ce_2O_3 is another stoichiometric phase with Ce^{3+} cations, where each Ce^{3+} cation is coordinated with seven oxygen an-

ions separated by 0.234 nm (3), 0.243 nm (1), and 0.270 nm (3), respectively. Thus, reduction of Ce^{4+} to Ce^{3+} may lead to local expansion. Volume expansion according to the reduction of CeO_2 was actually observed and it was attributed to larger ion diameter of Ce^{3+} than Ce^{4+} [1,4]. Hence, a local displacement including the second and third layer atoms at the line defect may occur, but NC-AFM observations cannot make this sort of conclusion. Major contribution of the geometry of constituent atoms to imaging of a reconstructed $CeO_2(0\,0\,1)$ surface by STM was also concluded by comparison with a theoretical calculation [14]. In our NC-AFM and STM measurements, multiple vacancies without local reconstruction were also observed as shown later.

3.3. Dynamic behavior of surface oxygen atoms

We have applied NC-AFM to monitor dynamic behavior of surface oxygen atoms on a slightly reduced $CeO_2(1\,1\,1)$ surface. From successive measurements of the same area of a $CeO_2(1\,1\,1)$ surface, it was observed that oxygen atoms could hop to the neighboring oxygen vacancy sites even at RT when multiple defects were not reconstructed [23]. Fig. 4(a) and (b) also show NC-AFM images of the same area of a slightly reduced $CeO_2(1\,1\,1)$ surface with non-reconstructed multiple defects observed at an interval of 182 s. The oxygen defect density was $(1.1–1.7) \times 10^{13}\,cm^{-2}$. Position of an oxygen vacancy in the multiple defect region (M) changed, indicating that oxygen atoms around the multiple defects hop to the neighboring site at RT. Point defects indicated as S in Fig. 4 did not change in 182 s. Again, positions of oxygen point vacancies on $CeO_2(1\,1\,1)$ surfaces with the low density of oxygen vacancies $((1.2–6.6) \times 10^{12}\,cm^{-2})$ did not change for more than 800 s. Further, multiple oxygen vacancies at reconstructed sites (marked as L_D in Fig. 4) were stable, where no structure changes were observed at RT. The hopping of oxygen atoms at the nonreconstructed multiple oxygen vacancies in Fig. 4 was always observed as a major event. The hopping direction did not have any correlation with the scanning direction. The hopping of oxygen atoms observed at RT occurs preferentially at metastable multiple defect structures which could not complete the local reconstruction during quenching from annealing temperature of 1173 K to RT.
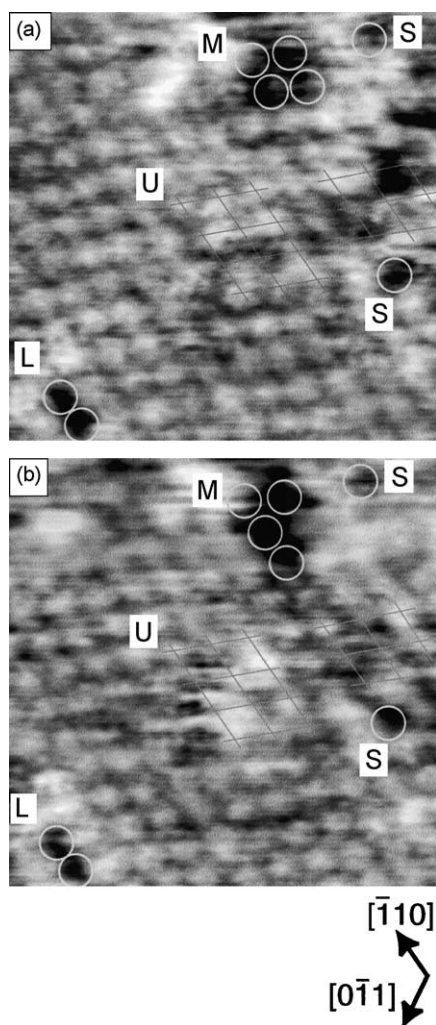
Fig. 4. Successive NC-AFM images (4.2 nm × 4.2 nm) of the same area of a slightly reduced CeO$_2$(1 1 1) surface with multiple defects observed at RT ($\Delta f \sim 263$ Hz). Time interval between (a) and (b) was 182 s. M and S are multiple and single oxygen vacancies. L$_D$ denotes a line defect with displaced oxygen atoms with brighter contrast. U represents a region where unstable oxygen atoms are observed.

CeO$_2$ is known as a prominent material for its high oxygen storage capacity depending on the oxidation states and used as a component of various catalysts as mentioned above. Diffusion coefficients and diffusion activation energies for oxygen atoms in bulk CeO$_{2-x}$ have been estimated by gas phase analysis during the exchange reaction of ^{18}O$_2$ with bulk ^{16}O above 1000 K by mass spectrometry [36] or by the depth profile analysis of the concentration of ^{18}O by secondary ion mass spectrometry (SIMS) [37]. A diffusion coefficient of stoichiometric CeO$_2$ is rather high at elevated temperatures among various oxides and the value becomes higher with reducing CeO$_{2-x}$ [1,36]. The static SIMS study on self-diffusion in nearly stoichiometric CeO$_2$ using labeled oxygen and cerium showed that surface oxygen atoms began to exchange with the bulk oxygen around 550 K, while Ce cations were immobile up to 900 K [38]. Thus, hopping of oxygen atoms on the CeO$_2$(1 1 1) surface at RT observed in Fig. 4 may be unexpected from the conventional view. Atom-resolved NC-AFM also imaged unstable oxygen atoms in the area (marked as U) in Fig. 4. We suppose that the oxygen atoms in this area fluctuate without positioning at fixed bulk-terminated sites, which may be induced by the presence of oxygen vacancies.

Fig. 5 shows successive STM observations of the same area on a slightly reduced CeO$_2$(1 1 1) surface with metastable multiple defects at 350 K. The oxygen defect density was (5.8–6.2) × 10^{13} cm^{-2}. In the region indicated as A and B, hopping of oxygen atoms was observed at an interval of 91 s. The increase of temperature caused much more prominent hopping of surface oxygen atoms over the whole surface observed by STM. The reconstructed multiple defects indicated as L$_D$ did not change during the STM observations. On a little more reduced CeO$_2$(1 1 1) (7.3–9.1% of oxygen vacancies that were mostly line defects), we have performed successive STM observations at an interval of 91 s per a flame at RT, 350 and 400 K, respectively. We estimated the temperature dependency though the time resolution was limited by a minimum tunneling current applicable in our STM system. The numbers of oxygen atoms (N) whose positions changed between the successive frames were counted and averaged per a second at each temperature, and plotted as a function of reciprocal temperature. This Arrhenius plot is shown in Fig. 6. The activation energy for the hopping process on the CeO$_2$(1 1 1) surface was calculated to be 30 kJ mol^{-1} and the pre-exponential factor was 2.0 × 10^4 s^{-1}. These results suggest that the hopping of oxygen on CeO$_2$(1 1 1) surface is a thermal process activated even at RT and not strongly affected by a scanning tip.

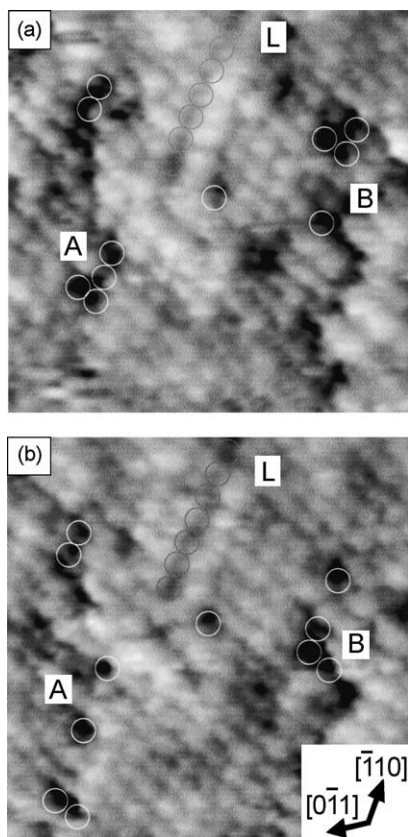If negatively charged oxygen atoms were postulated at an intermediate position in the hopping event

Fig. 5. Successive STM images (6.3 nm × 6.3 nm) of the same area of a slightly reduced $CeO_2(1\,1\,1)$ surface with multiple defects at 350 K. $V_s = -2.213$ V, $I_t = 23.3$ pA. Some multiple defects and point defects were healed by oxygen atoms in 91 s taken for scanning of the whole area of 13.4 nm × 13.4 nm. The oxygen vacancies were indicated by circles. In the regions of A and B, hopping of oxygen atoms was observed. L_D denotes a line defect with displaced oxygen atoms with brighter contrast.

and only Coulombic interaction is taken into consideration, multiple defects are energetically preferred to point vacancies due to less repulsion between surface oxygen atoms. Driving force of the oxygen hopping is probably repulsion between the first layer oxygen anions. To compensate local charge and maintain the driving force, a hopping oxygen may be a neutral atom that gives two electrons to two coordinated Ce^{4+} and receives two electrons from two Ce^{3+} at the original vacancy. The former process is similar to the formation of an oxygen vacancy by a thermal process. If such processes are the major issues, the different activation between multiple defects and a point vacancy
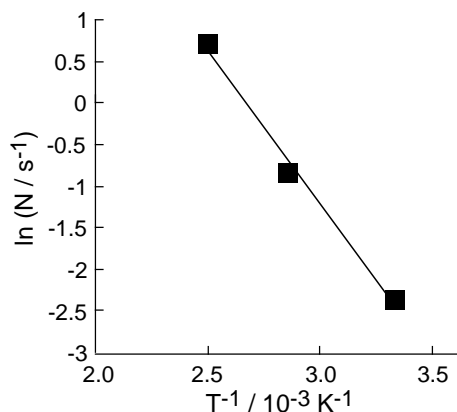

Fig. 6. Arrhenius plot for mobility of oxygen atoms (the number of displaced oxygen atoms (N) per second). Successive STM observations were performed at an interval of 91 s per a frame.

may not be explained. There should be another factor to control the oxygen hopping event. Further study is necessary to reveal criteria for oxygen hopping at unusually low temperature around RT.

Reoxidation of slightly reduced $CeO_2(1\,1\,1)$ surfaces was also examined. Fig. 7 shows successive NC-AFM images of a $CeO_2(1\,1\,1)$ surface under O_2 atmosphere (1.0×10^{-6} Pa) at RT. Fig. 7(a) was obtained immediately after oxygen dose. Dark regions indicated as M are multiple oxygen vacancies without local reconstruction. Exposure to O_2 healed the multiple oxygen vacancies and the healed sites showed bright contrasts with the (1×1) periodicity. The contrasts were similar to those for the surrounding oxygen atoms as shown in Fig. 7(b) and (c). Locations of oxygen vacancy sites visualized in Fig. 6(a)–(c) are also illustrated in Fig. 7(a′)–(c′). Thus, O_2 molecules dissociate to oxygen atoms at the multiple oxygen vacancies and the produced oxygen atoms heal the vacancies at RT. There are also minor point vacancies on the surface in Fig. 7(a). The oxygen point vacancies indicated as S were not healed by O_2 exposure for 91 s, but some of them were healed after 273 s under the O_2 ambient Fig. 7(c). Readsorption of oxygen on the point defects is much slower than that on the multiple defects. Healing of the oxygen vacancies by O_2 at RT is consistent with previous XPS and EELS studies [7,34]. The oxygen sticking probability at the oxygen vacancy sites was estimated to be 0.04 by the serial NC-AFM observation in Fig. 7. The fact that
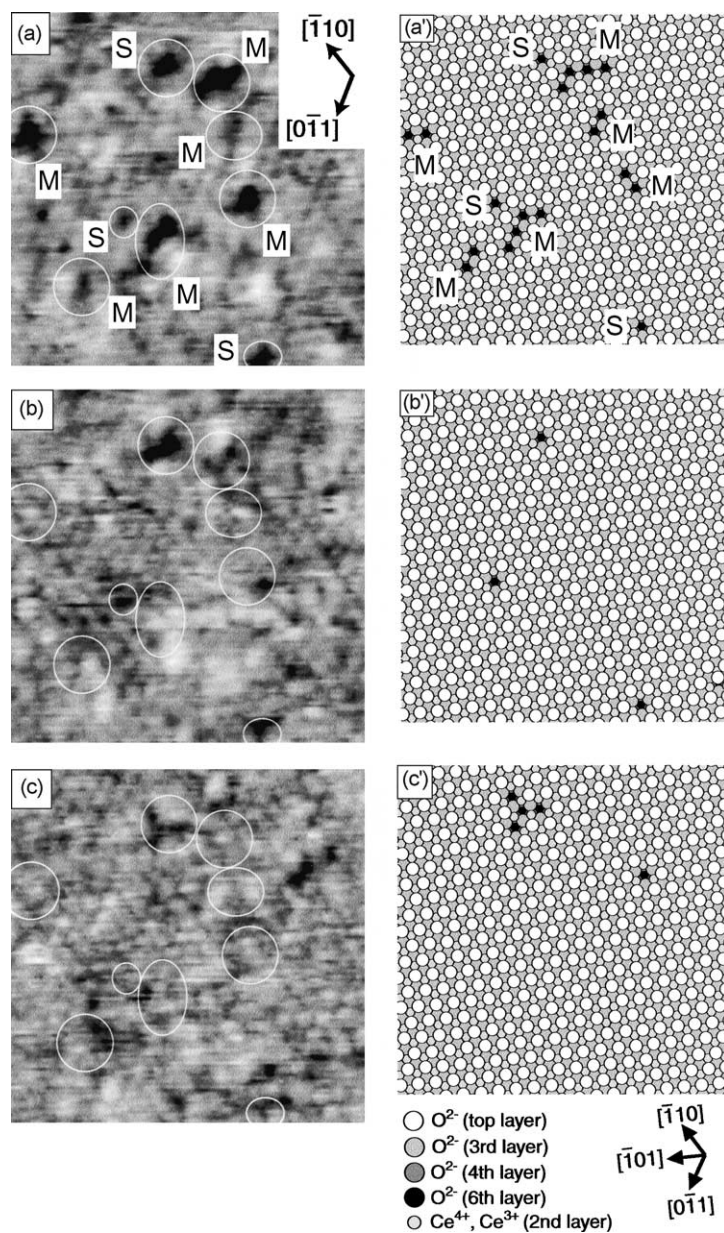
Fig. 7. Successive NC-AFM images (7.5 nm × 7.5 nm) of the same area of a slightly reduced CeO$_2$(1 1 1) surface with multiple defects under oxygen ambient (1.0 × 10^{-6} Pa) at RT ($\Delta f \sim 437$ Hz). Each frame was observed at (a) 0 s (immediately after O$_2$ dose), (b) 91 s, and (c) 273 s after O$_2$ exposure. Some multiple defects and point defects were healed by oxygen atoms in 91 s taken for scanning of the whole area of 10.3 nm × 10.3 nm. The same positions were indicated by white circles for a guide. M and S are multiple and single oxygen vacancies. The positions of oxygen vacancy sites observed in the successive images are shown in (a′)–(c′).

surface oxygen vacancies were healed and the oxygen atoms occupied the bulk-terminated positions with similar contrast to that for a stoichiometric surface observed in Fig. 1 demonstrates that the nearly stoichiometric $CeO_2(1\,1\,1)$ surface is O-terminated and each bright spot observed by NC-AFM corresponds to each surface oxygen atom. If the $(1\,1\,1)$ surface was cerium-terminated and if NC-AFM imaged each cerium atom, the same position as cerium vacancy could not be healed by oxygen because the cerium vacancy site is composed of only oxygen anions [23]. In the present study, facile reoxidation of the CeO_2 surface was confirmed on atomic scale.

3.4. Reactivity of surface oxygen atoms to methanol

Adsorption of methanol on CeO_2 layers grown on $Cu(1\,1\,1)$ and a $CeO_2(1\,1\,1)$ surface has been studied by Siokou and Nix [39] and Ferrizz et al. [40], respectively. They reported that methanol dissociated at RT and adsorbed at oxygen vacancy sites on the CeO_2 surface. Fig. 8 shows an atom-resolved image of a $CeO_2(1\,1\,1)$ surface after 4.5 L methanol exposure at RT. Before the exposure of methanol, only low protrusions (L) on oxygen atoms were observed as the height of 0.03–0.04 nm, which can be assigned as hydrogen adatom on surface oxygen atoms (Fig. 2). After exposure of methanol, high protrusions denoted as X and Y in Fig. 8 were observed as bright contrasts with a height of 0.06–0.08 nm. The high protrusions are considered as methoxy species (CH_3O) which were formed by dissociative adsorption of methanol. The density of oxygen vacancies decreased after the methanol exposure. The coverage of adsorbed methoxy was never larger than the oxygen defect density, which indicates that methanol adsorbs only on the defect sites. These results support the conclusion that the $CeO_2(1\,1\,1)$ surface is O-terminated. If the surface was Ce-terminated, defect sites would be exposed to three oxygen atoms, and the methoxy (CH_3O) cannot adsorb at the defect sites. The methoxy species did not adsorb at reconstructed line defects, which were stabilized due to the displacement of edge oxygen atoms surrounding the line defects as shown in Fig. 3(b). The methoxy (Y) is regarded to be methoxy species adsorbed at the oxygen vacancies with the molecular axis normal to
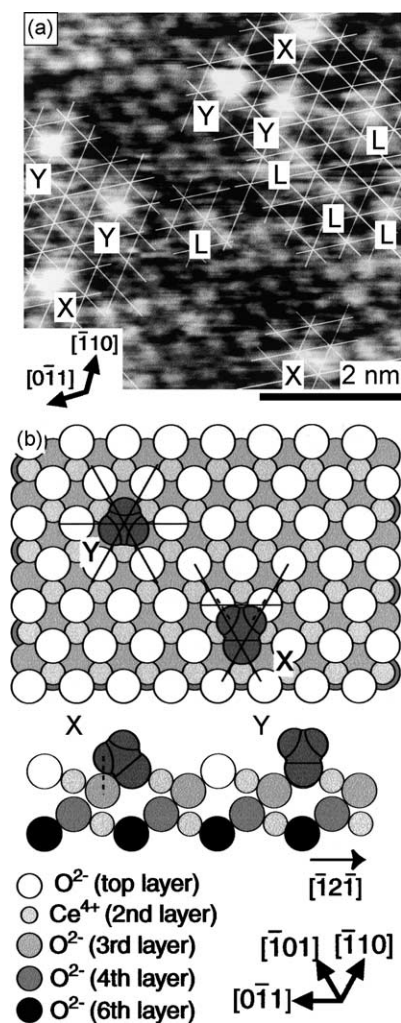

Fig. 8. (a) Atom-resolved NC-AFM image (5.3 nm × 5.3 nm) of a $CeO_2(1\,1\,1)$ surface after methanol exposure of 4.5 L. $\Delta f \sim 194\,Hz$. L shows hydrogen adatoms adsorbed on surface oxygen atoms. X and Y are methoxy species. (b) A structural model of adsorption sites of methoxy observed in (a). The bottom is a side-view of methoxy adsorbed on $CeO_2(1\,1\,1)$ surface in a diagonal of an unit cell ($[\bar{1}\,2\,\bar{1}]$ direction).

the surface. On the other hand, the bright contrasts for the methoxy (X) are located at threefold site of oxygen atoms, under which third-layer O^{2-} anions are present. If the adsorption of methoxy occurs over the oxygen threefold site, the height of methoxy species is allowed to be higher than that at the on-top site (Y), but it was not the case. Further, such methoxy should be unstable. Therefore, the atom-resolved NC-AFM
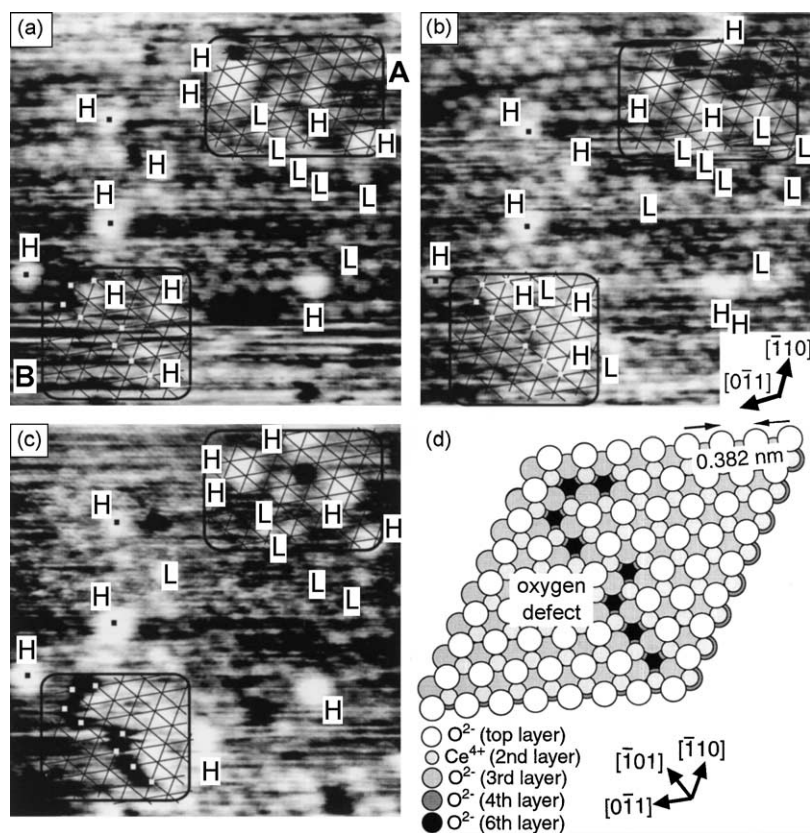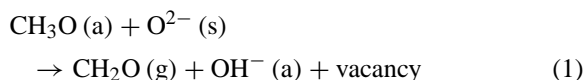
Fig. 9. (a)–(c) Successive atom-resolved NC-AFM images (6.5 nm × 6.5 nm) of a CeO$_2$(1 1 1) surface under methanol atmosphere (1.0 × 10^{-6} Pa) ($\Delta f \sim 209$ Hz). H and L are methoxy species and hydrogen adatoms, respectively. (d) A surface structural model of oxygen vacancies in the region B of (c).

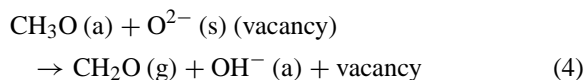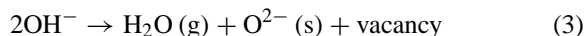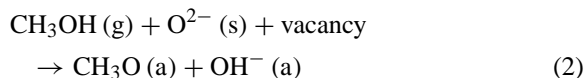images of methoxy species on the CeO$_2$(1 1 1) surface propose that methoxy species X and Y adsorb at oxygen vacancy sites and the methoxy X inclines to the threefold sites as shown in Fig. 8.

Finally, we have studied the reactivity of surface oxygen atoms to methanol by in situ NC-AFM measurements under methanol atmosphere. Fig. 9 shows successive atom-resolved NC-AFM images at the same area of a CeO$_2$(1 1 1) surface under methanol of 1.0 × 10^{-6} Pa. The frames in Fig. 9(a)–(c) were observed at 546, 728, and 819 s after methanol exposure, respectively. In the region denoted as A in Fig. 9, hydrogen atoms (L) were replaced by methoxy species (H), indicating the exchange reaction OH (a) + CH$_3$OH (g) → CH$_3$O (a) + H$_2$O (g). The reverse exchange CH$_3$O (a) + H$_2$O (g) → OH (a) + CH$_3$OH (g) was also observed. In the region
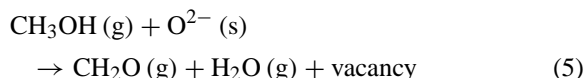
denoted as B, the successive NC-AFM observations revealed the formation of oxygen line defects at RT in Fig. 9(c). As there were no line defects in the region B of Fig. 9(a) and (b), it is indicated that the event took place within a time scale of 91 s between Fig. 9(b) and (c). The mechanism for the formation of oxygen vacancies induced by methanol is not clear at present, but it should be a kind of chain reaction mechanism to increase the number of oxygen vacancies. The methoxy species observed in the region B of Fig. 9(b) disappeared in Fig. 9(c). Thus, the following reaction pathways (1)–(4) are proposed. Once an oxygen vacancy at a specific site on the CeO$_2$(1 1 1) surface is produced as a slow step (1)

$$CH_3O\,(a) + O^{2-}\,(s)$$
$$\rightarrow CH_2O\,(g) + OH^-\,(a) + \text{vacancy} \qquad (1)$$

the following faster reactions (2)–(4) may propagate from the vacancy

$$CH_3OH\,(g) + O^{2-}\,(s) + vacancy$$
$$\rightarrow CH_3O\,(a) + OH^-\,(a) \qquad (2)$$

$$2OH^- \rightarrow H_2O\,(g) + O^{2-}\,(s) + vacancy \qquad (3)$$

$$CH_3O\,(a) + O^{2-}\,(s)\,(vacancy)$$
$$\rightarrow CH_2O\,(g) + OH^-\,(a) + vacancy \qquad (4)$$

where $CH_3O\,(a)$, $O^{2-}\,(s)$, $OH^-\,(a)$, $CH_2O\,(g)$, $CH_3OH\,(g)$, $H_2O\,(g)$, and $O^{2-}\,(s)$ (vacancy) represent adsorbed methoxy, surface oxygen atom, adsorbed hydrogen (hydroxyl), gaseous formaldehyde, gaseous methanol, gaseous water, and surface oxygen atom adjacent to the vacancy. Totally, these reactions (2)–(4) are represented as follows:

$$CH_3OH\,(g) + O^{2-}\,(s)$$
$$\rightarrow CH_2O\,(g) + H_2O\,(g) + vacancy \qquad (5)$$

These successive reactions proceed repeatedly to form the chain of oxygen defects. It was reported that methanol was oxidized to produce formaldehyde on $CeO_2(1\,1\,1)$ at 600–700 K by temperature programmed desorption (TPD) [40]. The present observation of methanol oxidation at RT by NC-AFM may be unexpected from the conventional view. Considering the density of the oxygen vacancy chain observed in Fig. 9 ($8.6 \times 10^{12}\,cm^{-2}$ (1.1% of top layer O^{2-})), it is not possible to detect the formaldehyde formation by mass spectrometry. The successive NC-AFM observations under methanol atmosphere indicate the high reactivity of the $CeO_2(1\,1\,1)$ surface even at RT.

4. Conclusions

$CeO_2(1\,1\,1)$ surface and its dynamic behavior were studied by atom-resolved NC-AFM and STM. It was concluded from the anisotropy of triangular vacancies, oxygen adsorption and methanol adsorption that the $CeO_2(1\,1\,1)$ surface is oxygen-terminated. Hexagonally arranged oxygen atoms, oxygen point vacancies, and a variety of structures of multiple oxygen vacancies were successfully visualized by NC-AFM and STM. At reconstructed multiple defects, edge oxygen atoms surrounding the multiple defects with enhanced brightness were displaced from the bulk-terminated positions. Surface oxygen defects could be healed by O_2 exposure at RT. Methanol adsorption was also observed at oxygen vacancy sites, the adsorption sites existed in two different species. Hopping of surface oxygen atoms at RT was observed at metastable multiple defects without enhancing the brightness of edge oxygen atoms. This was a thermally activated process. Successive NC-AFM observations under methanol atmosphere indicated a high reactivity of the $CeO_2(1\,1\,1)$ surface even at RT. Visualization of the atomic-scale structure and dynamic behavior of the CeO_2 surface by NC-AFM and STM provides a direct clue to understand the special oxygen storage capacity and surface reactivity.

References

[1] M. Mogensen, N.M. Sammes, G.A. Tompsett, Solid State Ionics 129 (2000) 63.
[2] A. Trovarelli, Catal. Rev. Sci. Eng. 38 (1996) 439.
[3] H.C. Yao, Y.F.Y. Yao, J. Catal. 86 (1984) 254.
[4] A. Trovarelli, Catalysis by Ceria and Related Materials, Imperial College Press, London, 2002.
[5] A.A. Bhattacharyya, G.M. Woltermann, J.S. Yoo, J.A. Karch, W.E. Cormier, Ind. Eng. Chem. Res. 27 (1988) 1356.
[6] A. Trovarelli, C. de Leitenburg, M. Boaro, G. Dolcetti, Catal. Today 50 (1999) 353.
[7] A. Pfau, K.D. Schierbaum, Surf. Sci. 321 (1994) 71.
[8] T. Chikyow, S.M. Bedair, L. Tye, N.A. El-Masry, Appl. Phys. Lett. 65 (1994) 1030.
[9] T.X.T. Sayle, S.C. Parker, C.R.A. Catlow, Surf. Sci. 316 (1994) 329.
[10] J.C. Conesa, Surf. Sci. 339 (1995) 337.
[11] H. Nörenberg, G.A.D. Briggs, Phys. Rev. Lett. 79 (1997) 4222.
[12] H. Nörenberg, G.A.D. Briggs, Surf. Sci. 424 (1999) L352.
[13] H. Nörenberg, G.A.D. Briggs, Surf. Sci. 433–435 (1999) 127.
[14] H. Nörenberg, G.A.D. Briggs, Surf. Sci. 477 (2001) 17.
[15] K. Fukui, H. Onishi, Y. Iwasawa, Phys. Rev. Lett. 79 (1997) 4202.
[16] H. Raza, C.L. Pang, S.A. Haycock, G. Thornton, Phys. Rev. Lett. 82 (1999) 5265.

[17] C.L. Pang, S.A. Haycock, H. Raza, P.J. Møller, G. Thornton, Phys. Rev. B 62 (2000) R7775.

[18] H. Hosoi, K. Sueoka, K. Hayakawa, K. Mukasa, Appl. Surf. Sci. 157 (2000) 218.

[19] C. Barth, M. Reichling, Nature 414 (2001) 54.

[20] Y. Sugawara, M. Ohta, H. Ueyama, S. Morita, Science 270 (1995) 1646.

[21] K. Fukui, Y. Iwasawa, Surf. Sci. 464 (2000) L719.

[22] K. Fukui, Y. Namai, Y. Iwasawa, Appl. Surf. Sci. 188 (2002) 252.

[23] Y. Namai, K. Fukui, Y. Iwasawa, J. Phys. Chem. B, in press.

[24] T.R. Alberecht, P. Grütter, D. Horne, D. Rugar, J. Appl. Phys. 69 (1991) 668.

[25] L. Howald, R. Lüthi, E. Meyer, H.J. Güntherodt, Phys. Rev. B 51 (1995) 5484.

[26] U. Berner, K. Schierbaum, Phys. Rev. B 65 (2002) 235404.

[27] H. Onishi, Y. Iwasawa, Chem. Phys. Lett. 226 (1994) 111.

[28] H. Onishi, K. Fukui, Y. Iwasawa, Bull. Chem. Soc. Jpn. 68 (1995) 2447.

[29] K. Fukui, H. Onishi, Y. Iwasawa, Chem. Phys. Lett. 280 (1997) 296.

[30] R. Tero, K. Fukui, Y. Iwasawa, J. Phys. Chem. B, in press.

[31] S. Suzuki, K. Fukui, H. Onishi, Y. Iwasawa, Phys. Rev. Lett. 84 (2000) 2156.

[32] K. Fukui, Y. Iwasawa, in: S. Morita, R. Wiesendanger, E. Meyer (Eds.), Noncontact Atomic Force Microscopy, Springer, New York, 2002, p. 167.

[33] V.E. Henrich, P.A. Cox, The Surface Science of Metal Oxides, Cambridge University Press, Cambridge, 1994.

[34] M. Romeo, K. Bak, J.E. Fallah, F.L. Normand, L. Hilaire, Surf. Interf. Anal. 20 (1993) 508.

[35] S. Morita, R. Wiesendanger, E. Meyer (Eds.), Noncontact Atomic Force Microscopy, Springer, New York, 2002.

[36] J.M. Floyd, Indian J. Technol. 11 (1973) 589.

[37] M. Kamiya, E. Shimada, Y. Ikuma, M. Komatsu, H. Haneda, J. Electrochem. Soc. 147 (2000) 1222.

[38] C.L. Perkins, M.A. Henderson, C.H.F. Peden, G.S. Herman, J. Vac. Sci. Technol. A 19 (2001) 1942.

[39] A. Siokou, R.M. Nix, J. Phys. Chem. B 103 (1999) 6984.

[40] R.M. Ferrizz, G.S. Wong, T. Egami, J.M. Vohs, Langmuir 17 (2001) 2464.